Phase-field-crystal simulation of nano-single crystal microcrack propagation under different orientation angles

Dunwei Peng(彭敦维)[1,2], Yunpeng Zhang(张云鹏)[1], Xiaolin Tian(田晓林)[2], Hua Hou(侯华)[2,3], and Yuhong Zhao(赵宇宏)[4,2,†]

[1] *School of Materials Science and Engineering, Xi'an University of Technology, Xi'an* 710048, *China*
[2] *School of Materials Science and Engineering, North University of China, Taiyuan* 030051, *China*
[3] *School of Materials Science and Engineering, Taiyuan University of Science and Technology, Taiyuan* 030024, *China*
[4] *Beijing Advanced Innovation Center for Materials Genome Engineering, University of Science and Technology Beijing, Beijing* 100083, *China*

(Received 31 August 2022; revised manuscript received 20 December 2022; accepted manuscript online 18 January 2023)

The propagation mechanism of microcracks in nanocrystalline single crystal systems under uniaxial dynamic and static tension is investigated using the phase-field-crystal method. Both dynamic and static stretching results show that different orientation angles can induce the crack propagation mode, microscopic morphology, the free energy, crack area change, and causing fracture failure. Crack propagation mode depends on the dislocation activity near the crack tip. Brittle propagation of the crack occurs due to dislocation always at crack tip. Dislocation is emitted at the front end of the crack tip and plastic deformation occurs, which belongs to ductile propagation. The orientation angles of 9° and 14° are brittle–ductile mixed propagation, while the orientation angles of 19° and 30° are brittle propagation and no dislocation is formed under dynamic tension. The vacancy and vacancy connectivity phenomenon would appear when the orientation angle is 14° under static tension, and the crack would be ductile propagation. While the orientation angle is 19° and 30°, the crack propagates in a certain direction, which is a kind of brittle propagation. This work has some practical significance in preventing material fracture failure and improving material performance.

Keywords: phase-field-crystal, microcrack, orientation angle, crack propagation

PACS: 46.50.+a, 61.72.Bb, 07.05.Tp **DOI:** 10.1088/1674-1056/acb41d

1. Introduction

Nanoscale microcracks are a kind of common defect in materials,[1] and their propagation mode affects the fracture behavior of materials,[2] mainly including brittle fracture,[3] and ductile fracture.[4] The existence of cracks destroys the continuity of the material, reduces the strength and plasticity of the material, and the stress concentration at the crack tip is easy to appear, and the fracture toughness and fatigue resistance of the material is reduced. Moreover, the fracture of the material shortens its service life and reduces the output of the product in the process of material processing and production. Therefore, the study of crack extension mechanisms helps to understand the evolution of material microstructures and provides theoretical support for preventing fracture failure and improving material properties.

To improve the quality and service life of materials, experts at home and abroad have conducted a lot of research and analysis on the crack-forming[5–9] and fracture failure[10] phenomenon of materials. The microstructure and fracture morphology of fatigue crack initiation and propagation of the alloy was observed using optical, scanning electron, and transmission electron microscopes. It can be observed that the crack initiation at the defect of the sample,[11] the crack propagation behavior in different alloys is significant discrepancy,[12] and so on. However, due to the limitations of environmental media, experimental preparation characterization and experimental cost in traditional experiments, it is difficult to observe the microstructure evolution process of metal materials to intuitively analyze the internal crack propagation of materials and to fundamentally reveal the microscopic mechanism of crack propagation at nanometer atomic scale and micron time scale.

Supposing that scholars intend to deeply analyze the mechanism of crack propagation, it is necessary to study the evolution process of crack propagation at the atomic scale. Molecular dynamics simulation as an effective tool to simulate microstructure defect evolution, including crack initiation and propagation. Decelis *et al.*[13] used Johnson and Morse potentials to simulate the crack tip formation of iron and copper by molecular dynamics simulation and studied the fracture behavior of brittle–ductile transition at the crack tip. Zhang *et al.*[14] analyzed the mechanism of dislocation nucleation, emission, deposition and formation of dislocation free zone during crack propagation in single crystal copper. Cao *et al.*[15] simulated the uniaxial tensile deformation process of single-crystal nickel material, and studied the crack generation and fracture process. However, for the microscopic defects in the material, the evolution process of them is 10^{-6} s, which is much larger than the atomic vibration time scale (10^{-14} s–10^{-12} s) of molecular dynamics. Moreover, molecular dynam-

†Corresponding author. E-mail: zhaoyuhong@nuc.edu.cn

© 2023 Chinese Physical Society and IOP Publishing Ltd

ics is mainly applicable to high stress (GPa) and high strain rate (10^7 s^{-1}–10^{10} s^{-1}), which is far behind the strain rate in 10 s^{-1}–10^3 s^{-1}. The phase–field–crystal (PFC) model reflecting the information on the diffusion time scale (10^{-6} s), makes up for this shortcoming, which fully reveals the influence of atomic effect. The PFC model[16] developed in recent years is the microscopic form of Cahn–Hilliard and Allen–Cahn equations[17–20] at the atomic scale, which can reflect the periodicity of the crystal lattice. This method characterizes the evolution of microstructure by constructing free energy equation and explores the effects of different processing techniques (temperature,[21,22] orientation angle,[23–25] strain mode, strain size, *etc.*) on the physical properties of metal structural defects, so as to make up for the deficiency of experiment.[26,27] The PFC model can predict and reduce the occurrence of dislocations and cracks at the atomic scale (10^{-9} m) and diffusion time scale (10^{-6} s), to improve the properties and prolong the service life of metal materials. Scholars have also done a lot of research on microcracks by using the PFC method. Elder *et al.*[28] conducted a preliminary exploration of the material microcrack propagation under the condition of uniaxial tensile stress. Gomez *et al.*[29] found that crack propagation was highly dependent on notch shape because different notch shapes lead to different stress concentrations.[30] In recent years, the PFC model has been used to discuss the propagation, bifurcation, and connectivity of microcracks,[31] the initiation and propagation of single and double cracks.[32] At the same time, the corresponding relationship between the initial crack shape, tensile mode,[33,34] strain size,[35] crystal orientation,[36] and the interaction of crack[37] and the crack growth were considered, as well as the influence of dislocation movement on the brittle–ductile transition behavior.[38]

In this paper, uniaxial dynamic tensile (DT) and static tensile (ST) are used to show the propagation details by observing the movement of atoms around the crack, and the influence of different orientation angles on the crack propagation mode is discussed. At the same time, the critical strain value of crack propagation under uniaxial ST is studied to reveal the propagation mechanism of cracks under different constant strains.

2. PFC model and calculation method

2.1. PFC model

2.1.1. System free energy function

Based on the Ginzburg–Landau theory, Elder[39] proposed the PFC method in 2002. The order parameter of this model is the conserved atomic density field. Referring to the energy function in the Swift–Hohenberg (SH) model,[40] the dimensionless system free energy function in the single-mode PFC model presented by Ref. [41] is

$$F = \int \mathrm{d}\boldsymbol{x} \left\{ \frac{\rho}{2} \left[r + \left(1+\nabla^2\right)^2 \right] \rho + \frac{\rho^4}{4} \right\}, \tag{1}$$

where F is the free energy function, ρ is the atomic density, $\boldsymbol{x}$ is the position vector, ∇^2 is the Laplace operator, r is a negative value, which represents the temperature of the system.

The single-mode approximate solution of the atomic density of the dimensionless triangular phase is

$$\rho = \rho_0 + A \left[\cos(qx) \cos\left(\frac{qy}{\sqrt{3}}\right) - \frac{1}{2} \cos\left(\frac{2qy}{\sqrt{3}}\right) \right], \tag{2}$$

where q is the wave vector, $A = \frac{4}{5}\left(\rho_0 + \frac{1}{3}\sqrt{-15r - 36\rho_0^2}\right)$, ρ_0 is the uniform atomic density distribution. The two-dimensional (2D) phase diagram of the single-mode PFC is shown in Fig. 1(a),[28] where S, T, and L represent strip phase, triangular phase, and liquid phase respectively, and the shadow part represents the coexistence area of two phases.

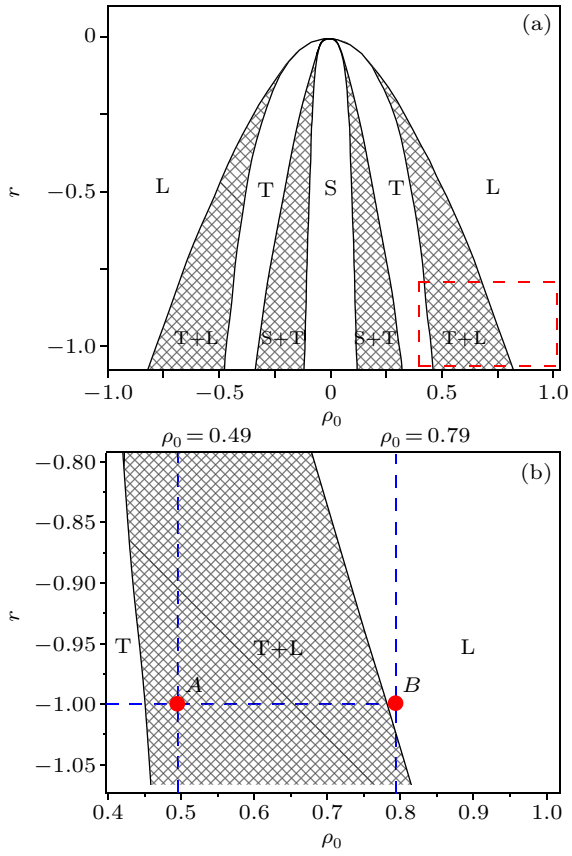


Fig. 1. (a) Two-dimensional phase diagram of PFC model,[28] (b) a larger version of the dotted box in panel (a).

2.1.2. Kinetic equation

The order parameter ρ of the dimensionless conservation field satisfies the Cahn–Hillard dynamic equation[28]

$$\frac{\partial \rho}{\partial t} = \nabla^2 \frac{\delta F}{\delta \rho} = \nabla^2 \left\{ \rho \left[r + \left(1+\nabla^2\right)^2 \right] + \rho^3 \right\}, \tag{3}$$

the semi-implicit Fourier method[42] is used to solve Eq. (3), and it is transformed into the Fourier space to obtain the atom density at the next moment:

$$\{\rho\}_{\boldsymbol{k},t+1} = \frac{\{\rho\}_{\boldsymbol{k},t} - \Delta t \boldsymbol{k}^2 \{\rho\}^3_{\boldsymbol{k},t}}{1 + \Delta t \boldsymbol{k}^2 \{\rho\}_{\boldsymbol{k},t+1} \left[r + \left(1 - \boldsymbol{k}^2\right)^2 \right]}, \tag{4}$$

where, $\{\rho\}_{\boldsymbol{k},t+1}$ and $\{\rho\}_{\boldsymbol{k},t}$ are the atomic densities corresponding to the Fourier space at $t+1$ and t, respectively; $\boldsymbol{k}^2$ is the Fourier spatial wave vector, and satisfies $\boldsymbol{k}^2 = |\boldsymbol{k}|^2$.

2.2. Parameter settings

In this simulation, the plane (111) in face-centered-cubic in the single crystal is taken as the research object (Figs. 2(a)–2(b)). The x axis is taken as the horizontal direction to characterize the $[\bar{1}10]$ crystal direction and the y axis is taken as the vertical direction to characterize the $[\bar{1}\bar{1}2]$ crystal direction. The crack growth model of three-dimensional (3D) face-centered cubic crystal is transformed into a 2D plane strain problem, choosing 2D lattices for numerical simulation.[43] To facilitate the analysis of the types of dislocations generated during crack propagation, the types of edge dislocations can be divided into six types according to the excess semi-atomic plane of edge dislocations, and the corresponding Burger vectors, as shown in Figs. 2(c)–2(d).

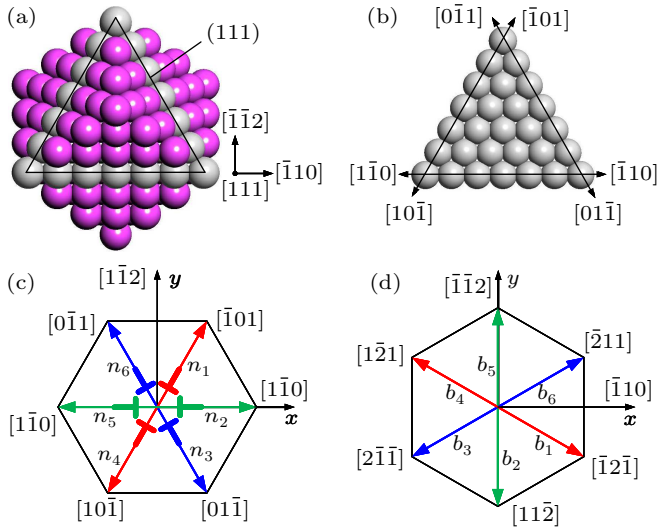


Fig. 2. (a) Face-centeredcubic lattice structure (111) planar atomic arrangement, (b) (111) planar crystal diagram, (c) blade dislocation type, (d) the corresponding Burgers vector type of panel (c).

2.2.1. Setting of the initial notch

In the 2D phase diagram of Fig. 1(a), the temperature parameter $r = -1.0$ and the atomic density parameter $\rho_0 = 0.49$ (point A in Fig. 1(b)) are selected, which are located in the coexistence zone of the triangular phase and liquid phase. In the prepared single crystal system, and the parameters at the initial crack are set to $r = -1.0$ and $\rho_1 = 0.79$ (point B in Fig. 1(b)), which can ensure that the crack is not swallowed by the triangular phase matrix in the simulation process.[44] The local amplification is shown in Fig. 3. The orientation angle is the angle θ between the atomic arrangement direction $[\bar{1}01]$ and the positive direction of x axis (taking 10° as an example). The parameters used in this study are dimensionless and do not involve the physical parameters of specific materials, and meet the periodic boundary conditions. Other parameters are shown in Table 1.

Table 1. Simulation parameters.

Calculation area grid	Initial rectangular crack size	Spatial step	Time step	Strain rate
$L_x \times L_y = 512\Delta x \times 512\Delta y$	$40\Delta x \times 10\Delta y$	$\Delta x' = \Delta y' = \pi/4$	$\Delta t = 0.3$	$\dot{\varepsilon} = 6 \times 10^{-6}/\Delta t$

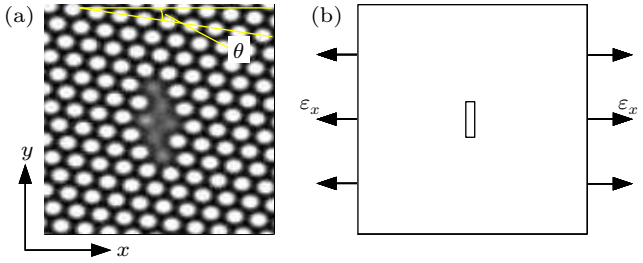


Fig. 3. Fracture morphology (a) initial crystal orientation angle is 10°, (b) systems of tensile strain along the x axis.

2.2.2. Applying deformation

This paper adopts two deformation methods, uniaxial DT and ST. The effect diagram of the applied strain is shown in Fig. 3(b). The coordinates of the grid point position in the system before and after deformation are (x, y) and (x', y') respectively. The specific formulas are shown below:

$$\text{Uniaxial DT}: \begin{cases} x' = x\,(1+\varepsilon_x) = x\,(1+n\dot{\varepsilon}\Delta t)\,, \\ y' = y, \end{cases} \tag{5}$$

$$\text{Uniaxial ST}: \begin{cases} x' = x\,(1+\varepsilon_x)\,, \\ y' = y. \end{cases} \tag{6}$$

When it is uniaxial DT, the spatial step length in the x direction increases with the strain rate at each time step $d = xn\dot{\varepsilon}\Delta t$, where $\dot{\varepsilon}$ is the dimensionless strain rate and n is the number of time steps. But in uniaxial ST, the tensile strain is a constant, the increment of space step is also a fixed value, which does not change with the change of time step.

3. Results and discussion

3.1. Crack propagation behavior under DT

3.1.1. Crack propagation at different orientation angles

According to the principle of minimum energy, the unstable factors in the system are eliminated after 20000 steps of relaxation. The free energy reaches the minimum, and the crystal structure tends to be stable, namely the system reaches equilibrium. The parameters used in the simulation are shown in Table 2. The samples with stable crystal structure (A1, B1, C1, D1) are dynamically stretched on the X axis to observe the simulated evolution morphology (Figs. 4–6).

When $\theta = 9°$, the microcracks in system A1 show the characteristics of expansion-turn-expansion with the continuous application of tensile strain during the expansion process in Fig. 4, and the critical strain value meets the Griffith fracture criterion.[45] In Fig. 4(a), the presupposed cracks area is

enlarged, but no crack propagation occurs. The main reason is that at the initial stage of applied strain, due to the stress concentration at the crack, the atomic lattice around the crack is staggered, and the distance between atoms is changed, but the strain did not reach the critical strain value. When $t^* = 45000$ ($\varepsilon_x = 0.27$), the accumulated stress at the crack tip exceeds the atomic binding force, and the crack propagates. In Fig. 4(b), the cracks continue to extend along the directions of $[\bar{1}01]$ and $[10\bar{1}]$, forming $\boldsymbol{n}_3$ ($[\bar{2}11]$) and $\boldsymbol{n}_6$ ($[2\bar{1}\bar{1}]$) dislocations (blue). At this time, plastic deformation occurs and stress concentration is released. When $\varepsilon_x = 0.318$, as shown in Fig. 4(d), the crack extends forward along the direction of $[\bar{1}01]$, resulting in $\boldsymbol{n}_2$ and $\boldsymbol{n}_5$ (green) new dislocations, which is a ductile extension. Until $t^* = 54000$ ($\varepsilon_x = 0.324$), as shown in Fig. 4(e). With the increase of strain, the dislocation at the tip of the crack occurs climbing and slipping motion, and the direction of crack growth changes due to dislocation plugging in the $[\bar{1}01]$ direction. It is worth noting that once the direction of crack propagation changes, the strain concentration decreases, and the Burgers vectors in the new direction of crack propagation are generated as $[1\bar{2}1]$ and $[\bar{1}2\bar{1}]$ $\boldsymbol{n}_1$ and $\boldsymbol{n}_4$ dislocations (red), so that the crack extends in $[01\bar{1}]$ and $[0\bar{1}1]$ directions. At the same time, the dislocation is always located at the crack tip. As the crack tip expands, it climbs and slides along the direction of its Burgers vector, which is a brittle propagation method. Due to the periodic boundary conditions, the same type of dislocations meets and annihilate. As shown in Fig. 4(f), $t^* = 58500$ ($\varepsilon_x = 0.351$), the crack extends to the edge of the simulation zone, and the crack is about to fracture. During the whole process, the crack propagates in a mixed mode of ductility and brittleness.

Table 2. Parameters used in the simulation.

Simulation scheme	Initial atomic density ρ_0	Notch atomic density ρ_1	Temperature r	Orientation angle θ (°)
A1	0.49	0.79	−1.0	9
B1	0.49	0.79	−1.0	14
C1	0.49	0.79	−1.0	19
D1	0.49	0.79	−1.0	30

When $\theta = 14°$, it can be seen from Fig. 5 that the propagation mode of microcracks in system B1 is similar to that in system A1 when $\theta = 9°$, and both of them show the characteristics of expansion-turn-expansion. At $t^* = 49000$ ($\varepsilon_x = 0.294$) the dislocation movement at the crack tip is blocked, causing dislocation plugging and crack steering so that the strain energy can be released. However, compared with Fig. 4, the generation time of dislocation pairs is earlier and the crack fracture is completed earlier, indicating that the larger the orientation angle is, the faster the propagation speed is. Wu *et al.*[46,47] performed molecular dynamics simulation on nickel-based single-crystal alloys with central cracks. The results show that the crack can expand rapidly and finally show brittle growth, the crack propagation rate slows down and the crack propagation changes from brittle to ductile. This result is consistent with our simulation results in Figs. 4 and 5. Rice and Thomson[48] proposed the criterion of dislocation emission at the crack tip, and confirmed that dislocation emission at the crack tip is one of the most basic processes to understand the ductile-brittle behavior of crystal materials. In 2004, Huang *et al.*[49] established a mechanical model to predict the critical criterion for the emission of dislocations at the blunt crack tip under mode I and II loading conditions, and calculate the corresponding stress intensity factor. At the same time, dislocation emission will also change the crack propagation mode, from brittleness to toughness.

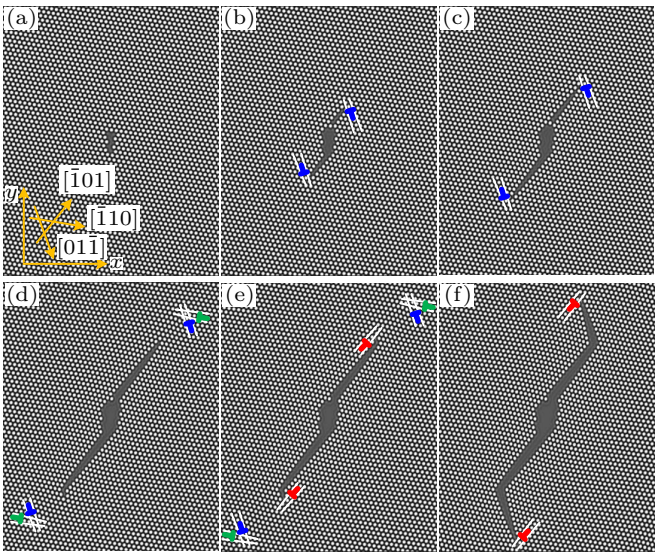


Fig. 4. Simulated evolution diagram of crack growth at strain applied to stage and $\theta = 9°$. (a) $t^* = 30000$, (b) $t^* = 45000$, (c) $t^* = 48000$, (d) $t^* = 53000$, (e) $t^* = 54000$, (f) $t^* = 58500$.

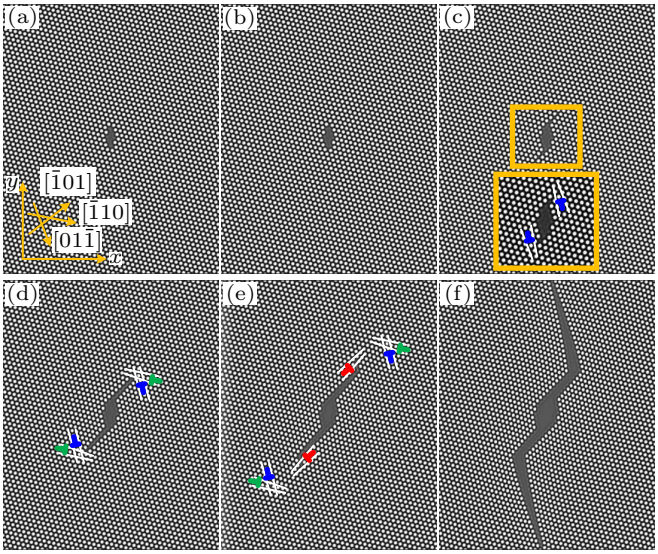


Fig. 5. Simulated evolution diagram of crack growth at strain applied to stage and $\theta = 14°$: (a) $t^* = 30000$, (b) $t^* = 35000$, (c) $t^* = 40000$, (d) $t^* = 45000$, (e) $t^* = 49000$, (f) $t^* = 57500$.

Figure 6 shows the simulation evolutions of the crack

propagation in systems C1 and D1, in which no dislocations are found during the crack propagation, this is consistent with the experiments.[50,51] Instead, the crack is torn along the orientations $[01\bar{1}]$ and $[0\bar{1}1]$, and brittle fracture occurs. When $\theta = 30°$, the propagation directions of the crack ($[01\bar{1}]$ and $[0\bar{1}1]$) are completely perpendicular to the x axis, indicating that under the tensile strain of the x axis, the atomic bonds in the directions of $[01\bar{1}]$ and $[0\bar{1}1]$ are broken and extends forward in the form of crystal surface cleavage until the sample fail.

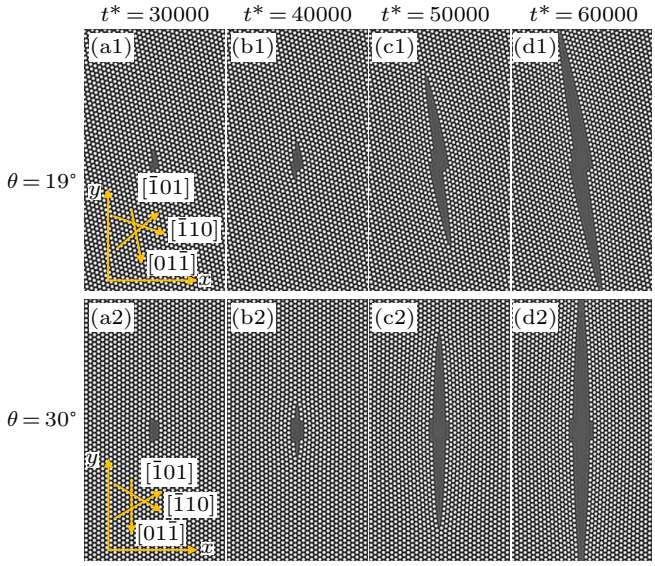


Fig. 6. Simulated evolution diagram of crack growth at stress applied stage and the $\theta = 19°$ and $\theta = 30°$, (a1)–(a2) $t^* = 30000$, (b1)–(b2) $t^* = 40000$, (c1)–(c2) $t^* = 51000$, (d1)–(d2) $t^* = 57000$.

3.1.2. Crack area and thermodynamic analysis

To explain the influence of orientation angle on crack growth rate and mode, the crack growth law and fracture mode are further revealed from the angle of system free energy and crack area.

The crack area (percentage of crack area to total area) curve represents changes with strain or time (Fig. 7(a)). the influence of orientation angle on the crack area has roughly the same trend, which increases slowly first and then rapidly in Fig. 7. Until $\varepsilon_x = 0.21$, the four groups of cracks begin to expand. The growth rate of the crack area with $\theta = 30°$ is the fastest, and the growth rate of crack with $\theta = 9°$ is the slowest. Figure 7(a) shows the fracture morphology of the four groups of samples, and the fracture time is $t^* = 5900$, $t^* = 57500$, $t^* = 56500$, $t^* = 55500$. The growth trends of crack area in the two groups of $\theta = 9°$ and $\theta = 14°$, $\theta = 19°$ and $\theta = 30°$ are completely consistent respectively. The former is a mixture of brittle fracture and ductile fracture, while the latter is brittle fracture. Figure 7(b) shows the atomic density distribution of different orientation angles at the same position ($Y = 256$) when $t^* = 57000$. The small fluctuation region of atomic density represents the crack region. The crack widths of $\theta = 9°$, 14°, 19°, 30° are $18\Delta x$, $21\Delta x$, $23\Delta x$, $29\Delta x$ respectively. In summary, under the same fracture mode, the crack growth area is sensitive to the size of the orientation angle, and increasing the orientation angle will accelerate the crack growth rate.

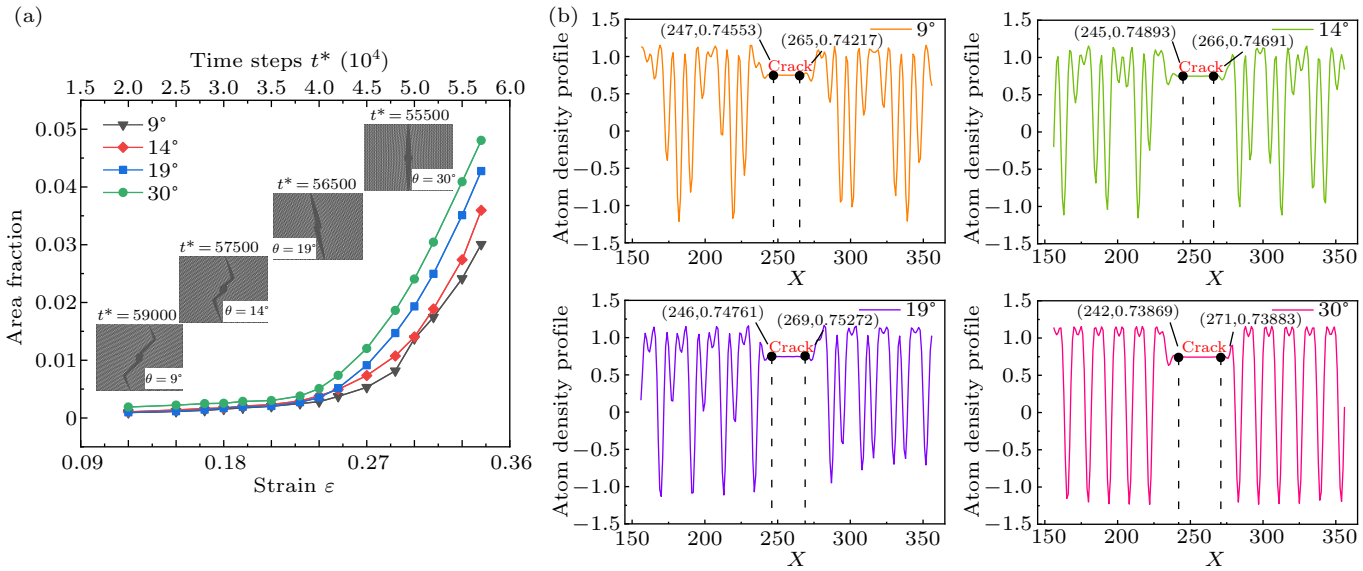


Fig. 7. (a) Influence of orientation angle on crack area fraction-strain; (b) $t^* = 57000$, atomic density distribution curve at the same position ($Y = 256$) with different orientation angles.

In the process of crack propagation, the free energy of the system also changes accordingly. Figure 8 shows the free energy curves of different orientation angles. Before fracture, the change trend of energy with time is basically the same. In the early and late stages of simulation, the change is relatively flat, while at the middle of the simulation, it rises rapidly. The free energy decreases from 20000 to 23000 because the residual stress in the body has not been completely eliminated. As the strain increase continuously, the energy curves of different orientation angles

gradually rise. However, it is found that the free energy of the system with crack propagation $\theta = 9°$ and $\theta = 14°$ in Fig. 8(a) and $\theta = 19°$ and $\theta = 30°$ in Fig. 8(b) increases in the same trend, and the energy reaches the lowest level at 23000. It can be seen from the corresponding crack propagation evolution diagram that under the same growth trend of free energy in the sample system, the corresponding crack propagation modes are also the same.

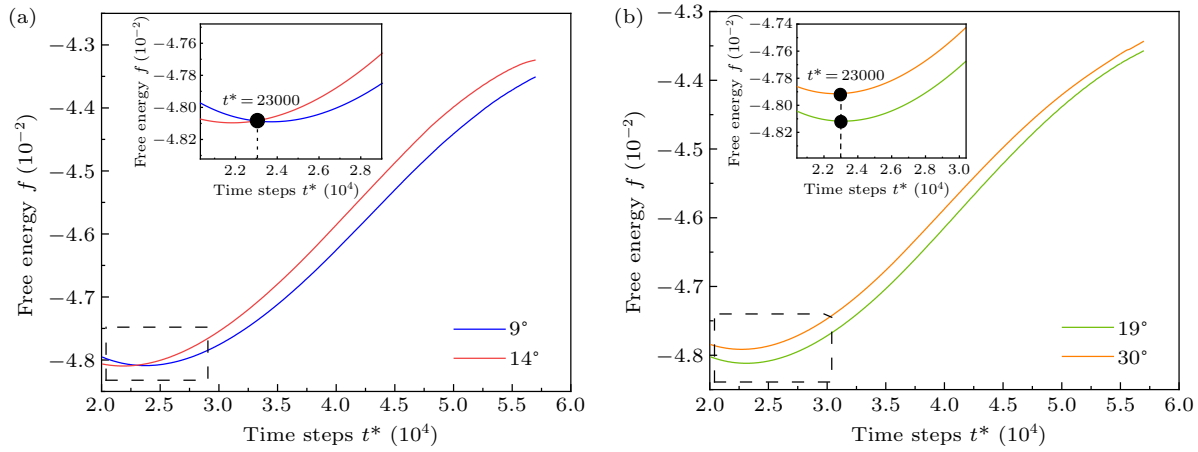


Fig. 8. Energy curves of different orientation angles (a) $\theta = 9°$ and $\theta = 14°$, (b) $\theta = 19°$ and $\theta = 30°$ over time.

3.2. Crack propagation behavior under ST

The influence of orientation angle on crack growth under uniaxial ST is studied. Different systems (A2, B2, C2, and D2) are selected for simulation. The specific parameters are set in Table 3.

Table 3. Parameters used in the simulation.

Simulation scheme	Initial atomic density ρ_0	Notch atomic density ρ_1	Temperature r	Orientation angle θ	Tensile strain ε_x (%)
A2	0.49	0.79	−1.0	9°	
B2	0.49	0.79	−1.0	14°	7, 8,
C2	0.49	0.79	−1.0	19°	9, 10
D2	0.49	0.79	−1.0	30°	

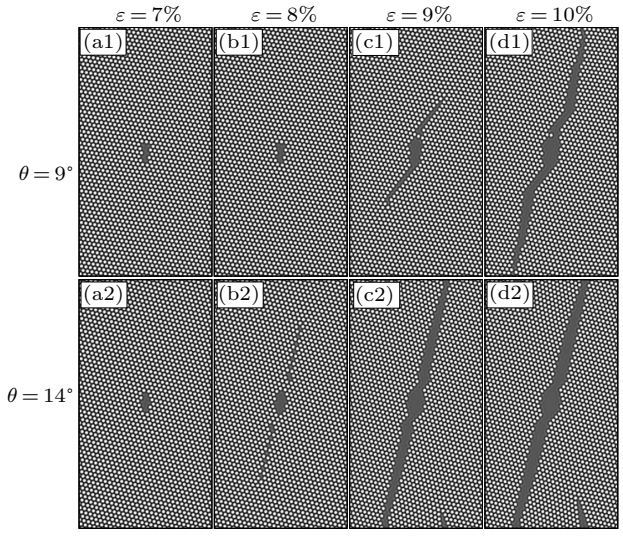


Fig. 9. Simulation of crack propagation under different tensile strains ($\varepsilon_x = 7\%$, $\varepsilon_x = 8\%$, $\varepsilon_x = 9\%$, $\varepsilon_x = 10\%$) at $t^* = 90000$ when $\theta = 9°$ and $\theta = 14°$.

Exploring the influence of orientation angle on the critical strain value of crack growth, and the crack growth conditions are studied ε_x of 7%, 8%, 9%, and 10%, respectively. When the external strain is larger, the growth rate of microcrack is faster, as shown in Figs. 9 and 10. It is found that the critical strain value of crack propagation is 9% for samples A2, C2, and D2, and 8% for sample B2. When $\varepsilon_x = 9\%$, the crack propagation rate increases with the increase of orientation angle.

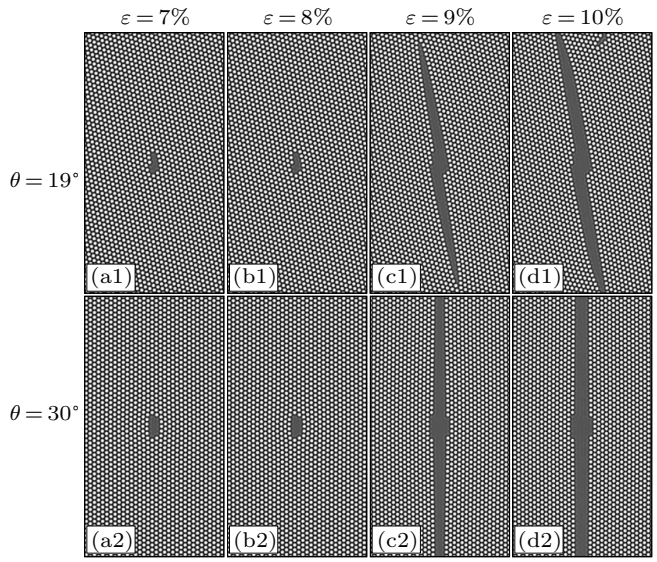


Fig. 10. The simulation diagram of crack propagation under different tensile strains ($\varepsilon_x = 7\%$, $\varepsilon_x = 8\%$, $\varepsilon_x = 9\%$, $\varepsilon_x = 10\%$) at $t^* = 90000$ when $\theta = 19°$ and $\theta = 30°$.

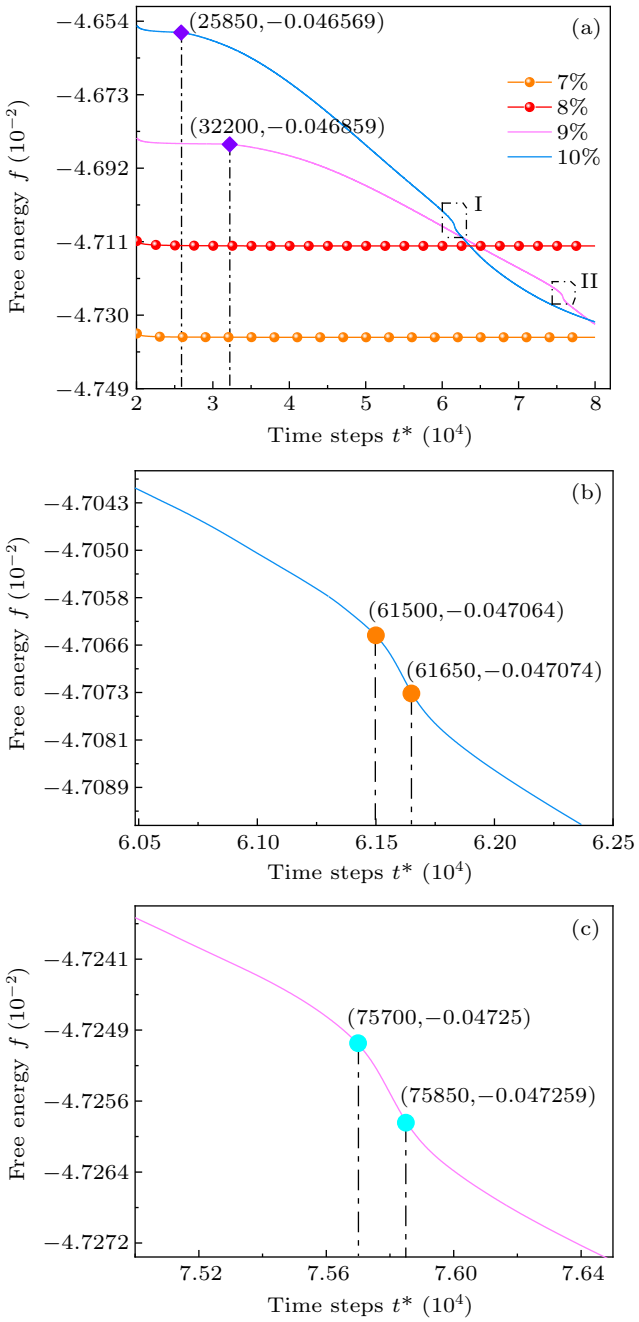


Fig. 11. (a) Curve diagram of energy changing with time under different strains with $\theta = 30°$, (b) partial enlargement of panel (a) I, (c) partial enlargement of panel (a) II.

It can be seen from Fig. 11(a) that when ε_x is small (7%, 8%), the energy curve is a straight line parallel to the x axis, and the crack does not expand. When the critical strain value reaches 9%, with the extension of time, the unexpanded energy curve of the crack before the initial stage $t^* = 32200$ is approximately a straight line parallel to the x axis, and the energy of the crack decreases continuously during the propagation. It can be seen from Fig. 11(c) that the crack is about to expand to the simulated area at the time $t^* = 75700$ and the energy drops sharply until the crack is completely fractured at the time $t^* = 75850$. When $\varepsilon_x = 10\%$, the changing trend of the curve is similar to that when $\varepsilon_x = 9\%$. The difference is that the crack propagates at $t^* = 25850$, and the energy drops sharply at $t^* = 61500$, and the crack completely breaks at $t^* = 61650$, as shown in Fig. 11(b). Compared with $\varepsilon_x = 9\%$, the crack initiation time is earlier and the propagation speed is faster.

By analyzing the critical strain of crack propagation at different orientation angles during static stretching, it is found that the critical strain of system B2 with is 8%, and the critical strain of system A2, C2, and D2 are all 9%, and the propagation modes are different. Therefore, the simulation evolution process of crack propagation is analyzed.

Figure 12 shows the crack dynamic evolution process when the $\theta = 14°$ and $\varepsilon_x = 8\%$. As $t^* = 55000$ (Fig. 12(a)), two dislocations are generated at both ends of the crack in the direction of Burgers vectors $[\bar{2}11]$ and $[2\bar{1}\bar{1}]$. As time goes on, at $t^* = 60000$ (Fig. 12(b)), the Burgers vector direction is $[\bar{1}\bar{1}2]$ and $[11\bar{2}]$ due to the generation of vacancies and new dislocations induced by dislocation motion. With the movement of the dislocation, the number of vacancies gradually increases (Fig. 12(c)). The atoms around the original vacancy are arranged neatly and there is no edge-type dislocation. A series of vacancies (Fig. 12(d)) are left in the direction of $[\bar{1}\bar{1}2]$ and $[11\bar{2}]$ not far from the crack tip, until the dislocation moves to the boundary of the simulated region. Due to the periodic boundary conditions, the same type of dislocations encounter and annihilation occurs, and the vacancies begin to connect to form serrated cracks. When it runs to $t^* = 13000$, it can be found in Fig. 12(e) that the crack formed by the vacancy communicates with the crack, and eventually leads to ductile fracture.[52–54] Meanwhile, the schematic diagram in Fig. 13 further explains that the mechanism of crack fracture caused by vacancy growth.

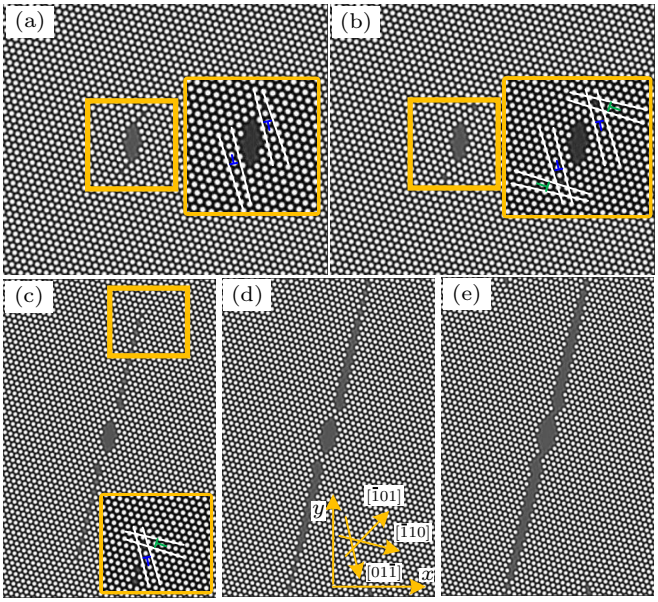


Fig. 12. The simulated evolution diagram of crack growth when $\theta = 14°$ and $\varepsilon_x = 8\%$: (a) $t^* = 55000$, (b) $t^* = 60000$, (c) $t^* = 100000$, (d) $t^* = 120000$, (e) $t^* = 130000$.

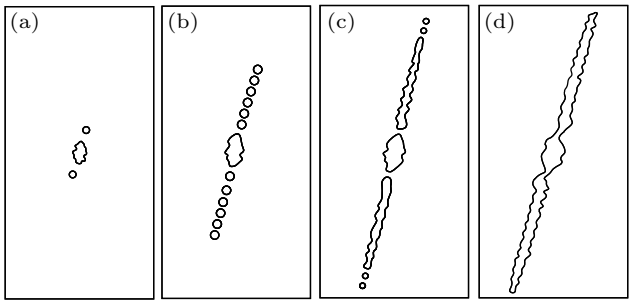


Fig. 13. Schematic diagram of fracture caused by spatiotemporal growth at $\theta = 14°$ and strain of 8%: (a) forming a vacancy, (b) vacant growth, (c) the vacancy begins to connect, (d) the vacancy completely coalesced and resulted in the fracture.

4. Discussion

According to Table 4 and Fig. 14, in the case of the same crack growth mode and equal strain, when the orientation angle is large, the crack propagation rate is faster and the fracture is earlier. When the orientation angle is equal, the greater the strain, the earlier the break time. It indicates that the increase of orientation angle and strain value can accelerate the crack propagation.

Table 4. Influence of orientation angle on fracture velocity of ST crack propagation.

Strain (%)	Ductile fracture		Brittle fracture	
	9°	14°	19°	30°
9	135000	80000	100000	75000
10	89000	65000	72000	61000

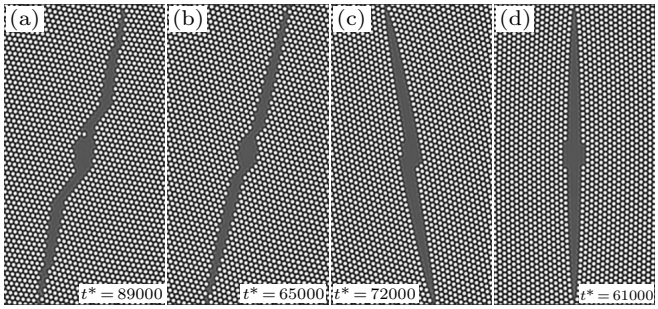


Fig. 14. When $\varepsilon_x = 10\%$, the fracture morphology of different orientation angles: (a) $\theta = 9°$, (b) $\theta = 14°$, (c) $\theta = 19°$, (d) $\theta = 30°$.

Figures 7(a) and 14 show the fracture morphology of cracks under DT and ST respectively. It is observed that under the condition of the same orientation angles (19° and 30°), the ST and DT methods are applied to the brittle propagation cracks, and it is found that the tensile method does not affect the crack growth morphology. However, when $\varepsilon_x = 0.09$ of ST, the system can be fractured. When the DT is carried out of $\varepsilon_x = 0.339$, and the fracture occurs. From the perspective of the whole evolution process, the crack propagation rate is faster under DT condition. When the $\theta = 9°$ and $\theta = 14°$, due to the dislocation pile-up, the expansion direction is changed during DT, and the expansion is in the mixed mode of ductile fracture and brittle fracture. In ST, vacancy is induced by dislocation, resulting in plastic deformation and vacancy connectivity, which is a typical ductile fracture.

5. Conclusion

In this paper, the phase-field-crystal model is used to study the effect of orientation angle on uniaxial dynamic and static tensile crack propagation. The results show below

(i) Under the uniaxial dynamic tensile condition, at the orientation angles of 9° and 14°, atom dislocations are formed around the cracks, and the cracks propagate in the manner of ductile fracture and brittle fracture. When $\theta = 19°$ and $\theta = 30°$, the notch cracks along a certain direction and the crack propagates in the form of brittle cleavage fracture.

(ii) Under the uniaxial static tensile state, the critical strain value is affected by the orientation angle. It can be found that when $\theta = 9°$, $\theta = 19°$, and $\theta = 30°$, the critical strain of the crack is 0.09; when $\theta = 14°$, the critical strain is 0.08, the dislocation induces the generation of vacancies and plastic deformation occurs with the evolution of time. With the continuous movement of dislocation, the number of vacancies gradually increases and begins to connect to form cracks. The crack connects with the main notch again, and finally leads to ductile fracture.

Acknowledgment

Project supported by the National Natural Science Foundation of China (Grant No. 52074246).

References

[1] Buehler M J, Abraham F F and Gao H J 2003 *Nature* **426** 141
[2] Pineau A, Benzerga A A and Pardoen T 2016 *Acta Mater.* **107** 424
[3] Kou M M, Lian Y J and Wang Y T 2019 *Eng. Fract. Mech.* **212** 41
[4] Shibanuma K, Hosoe T, Yamaguchi H, Tsukamoto M, Suzuki K and Aihara S 2018 *Eng. Fract. Mech.* **204** 434
[5] Liu G T and Yang L Y 2017 *Chin. Phys. B* **26** 094601
[6] Jiang L J and Liu G T 2017 *Chin. Phys. B* **26** 044601
[7] Guo H J, Liu Y H, Su Y N, Zhang Q L and Zhan G D 2020 *Chin. Phys. B* **29** 104602
[8] Guo L Y, Chen Z, Long J and Yang T 2015 *Acta Phys. Sin.* **64** 178102 (in Chinese)
[9] Liang J J, Gao N and Li Y H 2020 *Acta Phys. Sin.* **69** 116102 (in Chinese)
[10] Zheng Z Q, Cai B, Zhai T and Li S C 2011 *Mater. Sci. Eng. A-Struct.* **528** 2017
[11] Gope P C and Thakur A 2011 *Fatigue Fract. Eng. M* **34** 804
[12] Tanaka M, Tarleton E and Roberts S G 2008 *Acta Mater.* **56** 5123
[13] Decelis B, Argon A S and Yip S 1983 *J. Appl. Phys.* **54** 4864
[14] Zhang Y W, Wang T C and Tang Q H 1995 *Scripta Metal. Mater.* **33** 267
[15] Cao A J and Wei Y G 2007 *Phys. Rev. B* **76** 024113
[16] Tian X L, Zhao Y H, Peng D W, Guo Q W, Guo Z and Hou H 2021 *T. Nonferr. Metal. Soc.* **31** 1175
[17] Zhao Y H, Zhang B, Hou H, Chen W P and Wang M 2019 *J. Mater. Sci. Technol.* **35** 1044
[18] Chen W P, Zhao Y H, Yang S, Zhang D and Hou H 2021 *Adv. Compos. Hybrid Ma.* **4** 371
[19] Jing H X, Xing H, Dong X L and Han Y S 2022 *J. Electrochem. Soc.* **169** 032511
[20] Xing H, Dong X L, Sun D K and Han Y S 2020 *J. Mater. Sci. Technol.* **57** 26

[21] Qi K W, Zhao Y H, Guo H J, Tian X L and Hou H 2019 *Acta Phys. Sin.* **68** 170504 (in Chinese)
[22] Yamanaka A, Mcreynolds K and Voorhees P W 2017 *Acta Mater.* **133** 160
[23] Qi K W, Zhao Y H, Tian X L, Peng D W, Sun Y Y and Hou H 2020 *Acta Phys. Sin.* **69** 140504 (in Chinese)
[24] Guo H J, Zhao Y Y, Sun Y Y, Tian J Z, Hou H, Qi K W and Tian X L 2019 *Superlattice. Microst.* **129** 163
[25] Lu Y J, Gao Y J, Deng Q Q, Liu Z Y, Li Y X, Huang Z J and Luo Z R 2019 *Eur. Phys. J. B* **92** 1
[26] Xin T Z, Zhao Y H, Mahjoub R, Jiang J X, Yadav A, Nomoto K, Niu R M, Tang S, Ji F, Quadir Z, Miskovic D, Daniels J, Xu W Q, Liao X Z, Chen L Q, Hagihara K J, Li X Y, Ringer S and Ferry M 2021 *Sci. Adv.* **7** eabf3039
[27] Zhao Y H, Jing J H, Chen L W, Xu F H and Hou H 2021 *Acta Metall. Sin.* **57** 1107
[28] Elder K R and Grant M 2004 *Phys. Rev. E* **70** 051605
[29] Gomez H and Nogueira X 2012 *Comput. Method. Appl. M* **249–252** 52
[30] Stefanovic P, Haataja M and Provatas N 2006 *Phys. Rev. Lett.* **96** 225504
[31] Gao Y J, Luo Z R, Huang L L and Lin K 2013 *Chin. J. Nonferus. Met.* **23** 1892
[32] Huang L L, Gao Y J, Deng Q Q, Liu Z Y, Luo Z R, Li Y X and Huang Z J 2020 *Comput. Mater. Sci.* **173** 109413
[33] Liu Z Y, Gao Y J, Deng Q Q, Li Y X, Huang Z J, Liao K and Luo Z R 2020 *Comput. Mater. Sci.* **179** 109640
[34] Gao Y J, Deng Q Q, Huang L L, Ye L, Wen Z C and Luo Z R 2017 *Comput. Mater. Sci.* **130** 64
[35] Gao Y J, Luo Z R, Huang L L, Mao H, Huang C G and Lin K 2016 *Model. Simul. Mater. Sci.* **24** 055010
[36] Hu S, Chen Z, Peng Y Y, Liu Y J and Guo L Y 2016 *Comput. Mater. Sci.* **121** 143
[37] Hu S and Wang S 2019 *Physica B* **552** 104
[38] Hu S 2020 *Fatigue Fract. Eng. M* **43** 63
[39] Elder K R, Katakowski M, Haataja M and Grant M 2002 *Phys. Rev. Lett.* **88** 245701
[40] Swift J and Hohenberg P C 1977 *Phys. Rev. A* **15** 319
[41] Elder K R, Provatas N, Berry J, Stefanovic P and Grant M 2007 *Phys. Rev. B* **75** 064107
[42] Cheng M and Warren J A 2008 *J. Comput. Phys.* **227** 6241
[43] Morozov N F, Ovid'Ko L A, Sheinerman A G and Aifantis E C 2010 *J. Mech. Phys. Solids* **58** 1088
[44] Berry J, Elder K R and Grant M 2008 *Phys. Rev. B* **77** 224114
[45] Rountree C L, Kalia R K, Lidorikis E, Nakano A and Vashishta P 2002 *Ann. Rev. Mater. Res.* **32** 377
[46] Wu W P and Yao Z Z 2014 *Strength Mater.* **46** 164
[47] Wu W P and Yao Z Z 2012 *Theor. Appl. Fract. Mec.* **62** 67
[48] Rice J R and Thomson R 1974 *Philos. Mag.* **29** 73
[49] Huang M X and Li Z H 2004 *J. Mech. Phys. Solids* **52** 1991
[50] Saka H and Agata Y 2003 *Mater. Sci. Eng. A-Struct.* **350** 57
[51] Cao L X and Wang C Y 2006 *Chin. Phys. B* **15** 2092
[52] Tvergaard V and Hutchinson J W 2002 *Int. J. Solids Struct.* **39** 3581
[53] Li X D, Wang Y B, Chu W Y, Wang C and Bai C L 1998 *Sci. China Ser. E* **41** 411
[54] Zhu T, Li J and Yip S 2004 *Phys. Rev. Lett.* **93** 025503